

Synthesis of mixed-dimensional 1D-graphene nanoribbon/2D-CuSe heterostructures with controllable band alignments

Received: 4 March 2025

Accepted: 9 June 2025

Published online: 01 July 2025

Check for updates

Yong Zhang^{1,7}, Jianchen Lu^{1,7} , Lei Gao^{2,7} , Xin-jing Zhao^{3,4} , Gefei Niu¹, Xi Geng¹, Yi Zhang¹, Shicheng Li¹, Yuhang Yang¹, Yuan-Zhi Tan³, Shixuan Du⁵ & Jinming Cai^{1,6}

One- and two-dimensional (1D-2D) heterostructures have drawn growing interest due to their appealing optoelectronic and catalytic properties. Controlling the band alignment of 1D-2D heterostructures is crucial for their large-scale applications, but remains challenging to achieve experimentally. Here, we report a strategy for the atomically precise fabrication of 1D graphene nanoribbon (GNR) homojunctions and a variety of 1D-GNRs/2D-CuSe vertical heterostructures on Cu(111) substrate. By combining scanning tunneling microscopy, non-contact atomic force microscopy characterizations and density functional theory calculations, the entire preparative process is fully visualized. The GNR homojunctions, which bridge the Cu(111) substrate and the semiconducting CuSe monolayer, show a p-n junction characteristic. The hybrid heterostructures display various band alignments, achieved by varying the width and edge topologies of the GNRs, as well as controlling two different semiconducting phases of the CuSe monolayer. This work offers a promising method to precisely synthesize 1D/2D heterostructures with diverse band alignments for applications in high-performance nanodevices.

A van der Waals heterostructure (vdWHs) is formed by combining multiple materials through non-covalent bonds¹⁻³. Different from traditional heterostructures, vdWHs can combine the advantages of electronic, optical, thermal, and magnetic properties of different materials and has the potential to develop into the next generation of high-performance functional devices⁴⁻⁸. In particular, vdWHs constructed by one-dimension (1D) and two-dimension (2D) structures have recently attracted research interest. Studies have convincingly shown that such vdWHs will play a positive role in the development and application of future semiconductor devices⁹⁻¹¹.

As a well-known 1D structure, graphene nanoribbons (GNRs) have garnered significant attention in nanotechnology and materials science owing to their remarkable and inimitable properties tuned by atomically precise widths and edges¹²⁻¹⁵. In contrast to pristine graphene, a prominent trait of GNRs is their capacity to exhibit a bandgap, which can be finely tuned by varying the width and edge structures¹⁶⁻²⁵. This tunability renders GNRs highly prospective for applications in electronics, such as transistors, sensors, and even quantum dots²⁶⁻²⁸. Inspired by impurity-modulated or width-modulated lateral GNR heterojunctions²⁹⁻³² and tunable edge states in twisted bilayer zigzag

¹Faculty of Materials Science and Engineering, Kunming University of Science and Technology, Kunming 650093, China. ²Faculty of Science, Kunming University of Science and Technology, Kunming 650500, China. ³State Key Laboratory for Physical Chemistry of Solid Surfaces, Collaborative Innovation Center of Chemistry for Energy Materials, and Department of Chemistry, College of Chemistry and Chemical Engineering, Xiamen University, Xiamen 361005, China. ⁴Xiamen Key Laboratory of Optoelectronic Materials and Advanced Manufacturing, Institute of Luminescent Materials and Information Displays, College of Materials Science and Engineering, Huaqiao University, Xiamen 361021, China. ⁵Institute of Physics & University of Chinese Academy of Sciences, Chinese Academy of Sciences, Beijing, China. ⁶Southwest United Graduate School, Kunming 650093, China. ⁷These authors contributed equally: Yong Zhang, Jianchen Lu, Lei Gao. ✉ e-mail: jclu@kust.edu.cn; lgao@kust.edu.cn; zhaoxinjing@hqu.edu.cn; sxdu@iphy.ac.cn; j.cai@kust.edu.cn

GNR heterojunctions³³, vdWHs constructed by 1D GNR and 2D materials are promising for emerging properties.

Copper selenide (CuSe) monolayer which features a graphene-like honeycomb lattice and serves as a typical representative of 2D transition metal monochalcogenides, has been theoretically predicted to possess 2D Dirac nodal line fermions protected by mirror reflection symmetry³⁴. Depending on the chemical potential difference of selenium (Se) atoms, CuSe can form two distinct superstructures: 2D intrinsically patterned triangular nanopores with uniform size (nanopores CuSe, abbreviated as N-CuSe) and 1D moiré patterns (striped CuSe, abbreviated as S-CuSe)^{35–37}. The two superstructures exhibit as semiconductors with different bandgaps of 1.60 eV for the S-CuSe and 2.40 eV for the N-CuSe on Cu(111) substrate^{37,38}. Previous studies have demonstrated that both isolated CuSe monolayer and GNRs can be synthesized on identical Cu(111) substrates^{35–41}. It might be feasible to construct the GNRs/CuSe heterostructure by first growing GNRs on the Cu (111) surface and then growing the CuSe monolayer through intercalation. Through constructing 1D-GNRs/2D-CuSe vdWHs, one can expect to combine the features of GNRs distinctive properties (such as tunable band gaps) with the advantageous characteristics of the CuSe monolayer, including high electrical conductivity⁴². These combined features hold significant promise in the future landscape of nanotechnologies, particularly in ultra-high-speed/gain broadband photodetectors and next-generation atomically thin transistors with exceptional flexibility^{9–11}.

In this work, we propose an atomically precise synthetic strategy for synthesizing GNRs homojunction and GNRs/CuSe heterojunction on a Cu(111) substrate. The synthesis pathway employs a hierarchical growth strategy. Firstly, we choose the quateranthracene (QA) precursor as a building block for the synthesis of GNRs-1 on the Cu(111), as shown in Fig. 1a. Then, depositing of Se atoms onto the

GNRs-1/Cu(111) sample. Upon thermal annealing, a reaction occurs between the Se atoms and the Cu atoms from the substrate, which leads to the formation of a CuSe monolayer. As the amount of Se deposition increases, the above sample undergoes three discernible phases, as shown in Fig. 1b. In the first phase, GNRs-1 bridge across both the Cu(111) and the S-CuSe, giving rise to GNRs-1 homojunctions. In the second phase, GNRs-1 are situated atop the S-CuSe monolayer, leading to the formation of GNRs-1/S-CuSe vdWHs. In the third phase, GNRs-1 are positioned above the N-CuSe monolayer, giving rise to GNRs-1/N-CuSe vdWHs. By means of scanning tunneling microscopy (STM), non-contact atomic force microscopy (NC-AFM) characterizations and density functional theory (DFT) calculations, we visualize the entire growth process described above. Scanning tunneling spectroscopy (STS) is employed to probe the band arrangements of GNRs-1 homojunctions, GNRs-1/S-CuSe and GNRs-1/N-CuSe vdWHs. Furthermore, we construct two additional GNRs/CuSe heterostructures, confirming the universality of this strategy and enhancing the band arrangement and potential applications of these heterostructures.

Results and discussion

Synthesis of GNRs-1 homojunction

Initially, QA molecules are deposited onto a Cu(111) substrate maintained at room temperature, leading to the formation of a large-scale porous self-assembly (Supplementary Fig. 1). When the sample undergoes thermal annealing at 160 °C, the QA molecules experience C–H activation and then transform into 1D polymers. The mechanism and specific details regarding the C–H activation process for QA molecules are presented (Supplementary Fig. 2). Subsequently, when the sample is annealed to a higher temperature of 250 °C, the polymers are further converted into conjugated GNRs-1 through cyclodehydrogenation (Fig. 1c). It is noteworthy that the synthesized GNRs-1 are

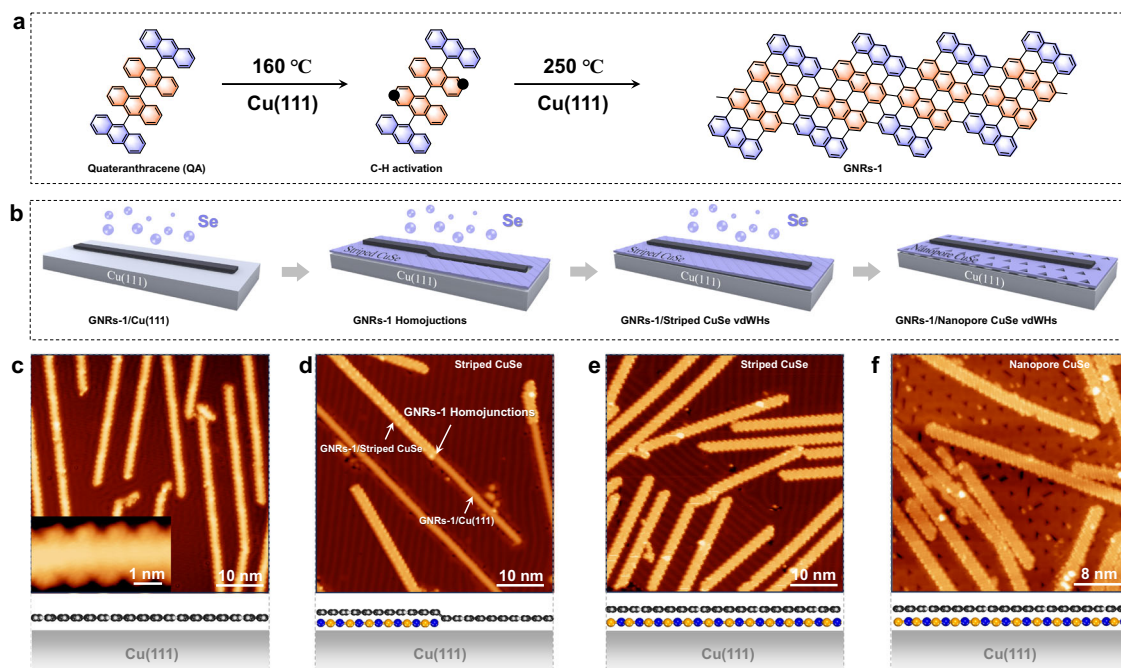


Fig. 1 | Schematic illustration and large-scale scanning tunneling microscopy (STM) images of the stepwise fabrication of multiple graphene nanoribbons (GNRs) and CuSe heterojunctions. **a** Schematic representation of the synthesis method of GNRs-1 using quateranthracene (QA) precursor. **b** Schematic representation of the stepwise fabrication of multiple GNRs-1/CuSe heterostructures. **c** GNRs-1 on Cu(111) substrate. The inset of (c) shows the high-resolution STM image of GNR-1. The bottom structural model presents the side view of GNRs-1 on the Cu(111) surface. (Voltage = 0.5 V, I-setpoint = 120 pA; inset image: Voltage = 0.2 V,

I-setpoint = 120 pA). **d** GNRs-1 homojunctions. The bottom structural model presents the side view of GNRs-1 homojunctions on the Cu(111) surface. (Voltage = 0.8 V, I-setpoint = 50 pA). **e** GNRs-1/Striped-CuSe heterojunctions. The bottom structural model presents the side view of GNRs-1/Striped-CuSe heterojunctions. (Voltage = 0.5 V, I-setpoint = 80 pA). **f** GNRs-1/Nanopore-CuSe heterojunctions. The bottom structural model presents the side view of GNRs-1/Nanopore-CuSe heterojunctions. (Voltage = 0.8 V, I-setpoint = 50 pA).

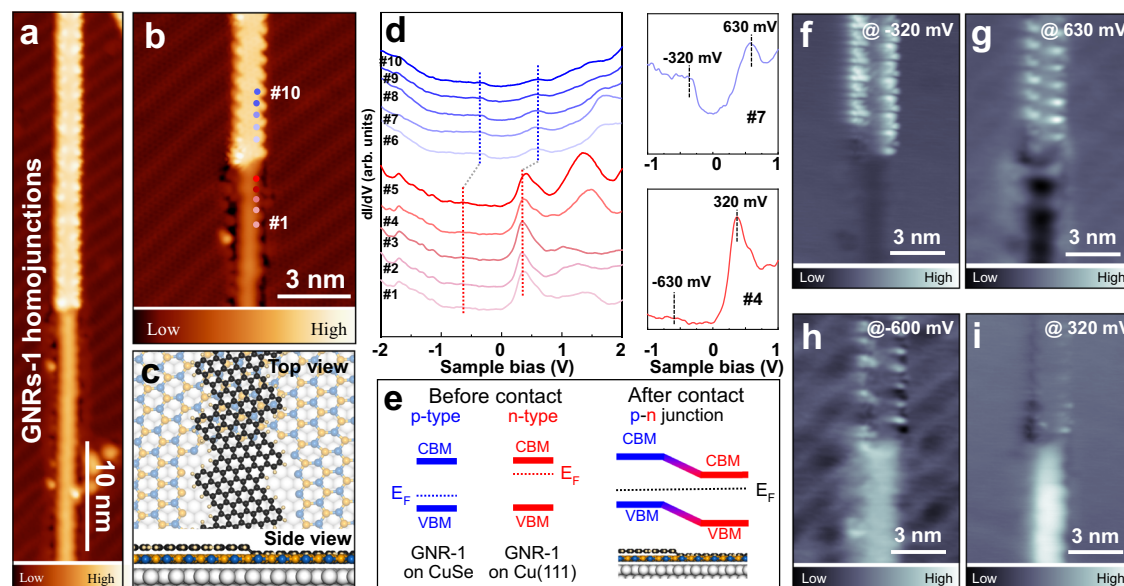


Fig. 2 | Electronic properties of GNRs-1 homojunctions. **a** STM image of GNRs-1 homojunction (Voltage = 0.8 V, I-setpoint = 50 pA). **b** High-resolution STM image of GNRs-1 homojunction (Voltage = -0.35 V, I-setpoint = 120 pA). **c** Structure model of GNRs-1 homojunction. **d** Differential conductance (dI/dV) spectra of the GNRs-1 taken across the GNRs-1 homojunctions as indicated by colored dots in **(b)**. The

insets represent the zoom-in dI/dV spectra of #4 and #7, respectively. The vertical dashed lines represent the positions of the conduction band and the valence band in the dI/dV spectra. **e** Schematic diagram of the staggered band alignment in GNRs-1 homojunction (E_F represents the position of the Fermi energy level). **f–i** dI/dV maps of GNRs-1 homojunction at a given bias voltage.

of high quality, with an average length exceeding 60 nm. High-resolution STM and NC-AFM images clearly display the detailed structure of these GNRs-1 (Supplementary Fig. 3).

Next, Se atoms are deposited onto the sample mentioned above, and then the sample is annealed to 220 °C. Interestingly, we found that Se atoms easily react with copper atoms from Cu(111) substrate. This interaction, potentially involving interfacial diffusion, leads to the spontaneous formation of a semiconducting CuSe monolayer. (Supplementary Fig. 4)^{35,38}. At relatively low coverage of Se atoms, the S-CuSe appears in the form of isolated islands that are separated by GNRs-1, and its binding with GNRs-1 is through weak vdW interactions, which is verified by the high-resolution STM (Supplementary Fig. 5).

When the deposition amount of Se atoms continues to increase and additional annealing is carried out, the Se atoms start to intercalate between a part of the GNRs-1 and the copper substrate. Afterwards, these Se atoms react with Cu atoms beneath the GNRs-1 to form an S-CuSe monolayer, which elevates a part of GNRs-1 and gives rise to the formation of the GNRs-1 with S-CuSe monolayer intercalation. As can be seen in Figs. 1d and 2a, one part of a GNRs-1 is positioned on the S-CuSe monolayer, while the other end remains on the Cu(111) surface. Notably, when compared to GNRs-1 on Cu(111), those on the S-CuSe monolayer exhibit greater brightness and width (as marked by arrows in Fig. 1d). The measured GNRs-1 width on the S-CuSe monolayer is about 1.90 ± 0.5 nm, while the width of GNRs-1 on Cu(111) substrate is about 1.65 ± 0.5 nm, as shown in Supplementary Fig. 6. This morphological difference can be attributed to the electron decoupling effect of GNRs on CuSe, as previously published literatures^{20,41}. A high-resolution STM image in Fig. 2b provides a detailed visualization of the microscopic morphology of GNRs-1 after the intercalation process. The atomically precise structure of GNRs-1, free from defects or impurities, indicates that GNRs-1 remain intact during the formation of S-CuSe monolayer. Figure 2c presents the DFT optimized structural model with one end of a single GNRs-1 lies on the S-CuSe monolayer and the other end on the Cu(111) substrate.

Subsequently, we proceed to investigate the electronic properties of a single GNRs-1 that has one end located on the S-CuSe monolayer

and the other on the Cu(111) substrate. The dI/dV spectra (Nos. #1 to #5), as presented in Fig. 2d and Supplementary Fig. 7, are acquired at the GNRs-1 on the Cu(111) substrate. The zoomed-in dI/dV spectrum (Nos. 4#), depicted in red color, reveals the representative density of state distribution of GNRs-1 near the Fermi level on the Cu(111). Specifically, two peaks can be clearly identified, with a conduction band minimum (CBM) at 320 mV and a valence band maximum (VBM) at -630 mV, resulting in an average electronic bandgap of 0.95 eV for as-synthesized GNRs-1 on the Cu(111) (For more detailed dI/dV spectra of GNRs-1 on the Cu(111) substrate, please refer to Supplementary Fig. 8). Furthermore, the dI/dV spectra (Nos. #6 to #10) are collected from GNRs-1 on the S-CuSe monolayer. The zoomed-in dI/dV spectrum (Nos. 7#), highlighted in sky-blue, illustrates the characteristic density of state distribution of GNRs-1 near the Fermi level on the S-CuSe. Two distinct peaks are noticed, with the CBM at 630 mV and the VBM at -320 mV, leading to an average bandgap of 0.95 eV for as-synthesized GNRs-1 on the S-CuSe monolayer. When comparing the GNRs-1 on the Cu(111) and that on the S-CuSe, although the bandgap of the GNRs-1 remains mostly unchanged, the entire band structure is shifted slightly to the right. This shift indicates the formation of a homojunction with staggered band alignment based on GNRs-1.

Figure 2e shows the schematic diagram of the band alignment in GNRs-1 homojunction. The Fermi level (E_F) of GNRs-1 on Cu(111) is closer to the CBM than to the VBM, which demonstrates that GNRs-1 on the Cu(111) substrate is a n-type semiconductor. In contrast, the E_F of GNRs-1 on the S-CuSe monolayer is closer to the VBM than to the CBM, indicating that GNRs-1 on S-CuSe is a p-type semiconductor. When a GNRs-1 extends across both the Cu(111) substrate and the S-CuSe monolayer, a GNRs-1 homojunction is formed. As the charge continues to flow within this structure, the E_F of GNRs-1 on Cu(111) and GNRs-1 on S-CuSe eventually align to the same level. During this alignment process, electrons are transferred from the n-type GNRs-1 on Cu(111) to the p-type GNRs-1 on S-CuSe. This transfer of electrons generates an electric field (E_{in}) near the homojunction contact area, which points from the n-type GNRs-1 on Cu(111) towards the p-type GNRs-1 on S-CuSe. (For a more detailed band alignment analysis, please refer to Supplementary Fig. 9). Additionally, it is found that the width of the

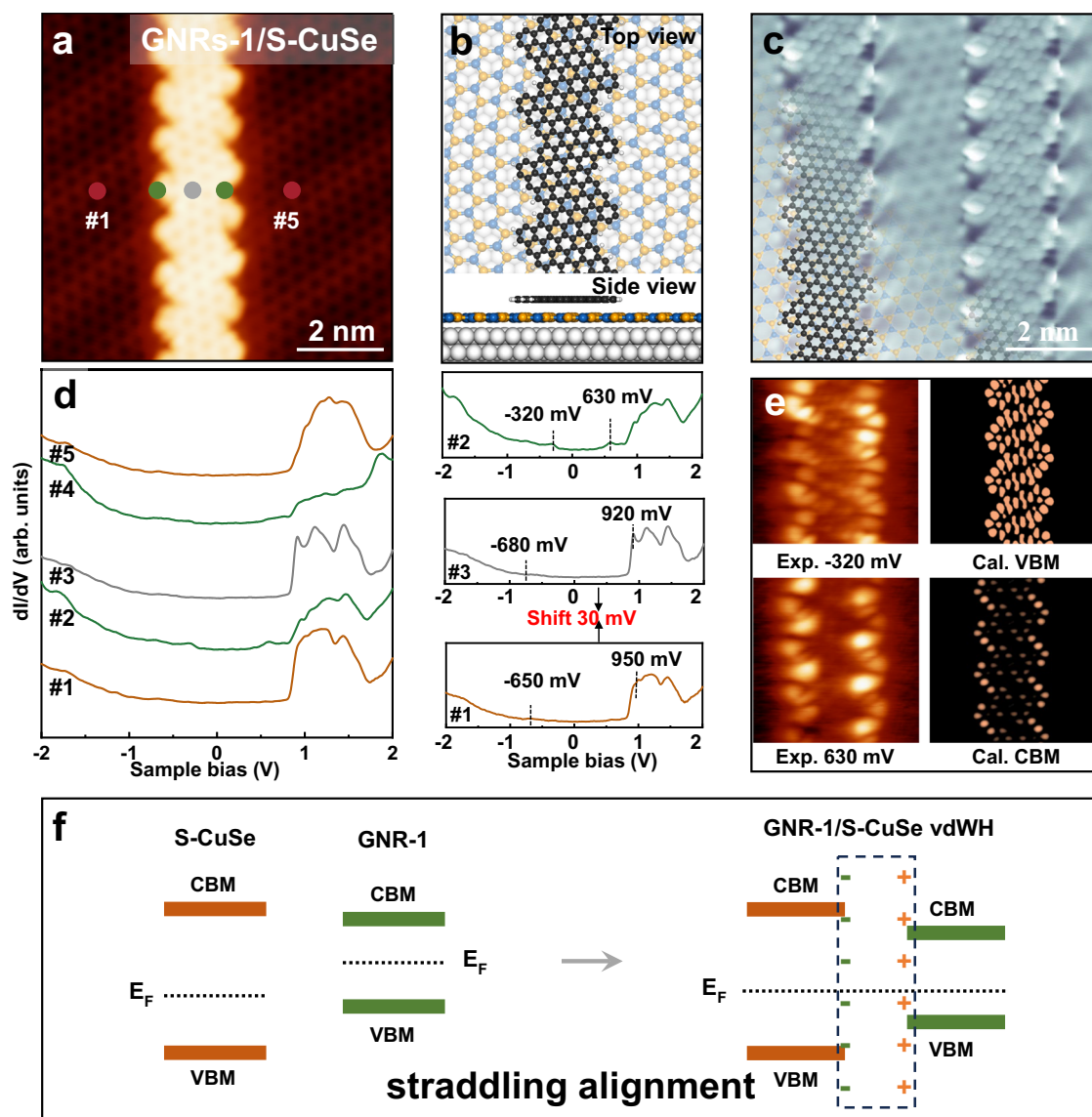


Fig. 3 | Structure and electronic properties of GNRs-1/Striped-CuSe van der Waals heterostructures (vdWHs). **a, b** High-resolution STM image and structure model of GNRs-1/S-CuSe vdWHs, respectively (Voltage = 0.2 V, I-setpoint = 120 pA). **c** Bond-resolved STM image of GNRs-1/S-CuSe vdWHs (Voltage = 5 mV, I-setpoint = 120 pA). **d** dI/dV spectra of GNRs-1/S-CuSe vdWHs acquired at the colored dots in (a). The insets represent the zoom-in dI/dV spectra of #1, #2 and #3, respectively.

The vertical dashed lines represent the positions of the conduction band and the valence band in the dI/dV spectra. **e** Experimental and calculated dI/dV maps obtained at given bias voltages for GNRs-1/S-CuSe vdWHs. CBM and VBM represent the conduction band minimum and the valence band maximum, respectively. **f** Schematic band-diagram illustration of GNRs-1/S-CuSe vdWHs. The + and - signs in dashed box represent positive and negative charges, respectively.

depletion region is -1.30 nm (Supplementary Fig. 10). Away from the homojunction contact area, GNRs-1 maintains its intrinsic semi-conducting properties, behaving as an n-type on Cu(III) and a p-type on S-CuSe, while their Fermi levels remain unchanged.

The spatial electronic state distributions of the GNRs-1 homojunction at different bias voltage are experimentally explored using dI/dV maps. Figure 2f, g respectively displays the dI/dV maps obtained at bias voltage of -320 mV and 630 mV for the GNRs-1 homojunctions depicted in the Fig. 2b. These maps disclose significant electronic state distributions along the edge of the GNRs-1 on the S-CuSe monolayer, while no remarkable electronic state distribution can be noticed for the GNRs-1 on the Cu(III) substrate. Figure 2h, i present the dI/dV maps acquired at bias voltage of -600 mV and 320 mV respectively for the GNRs-1 homojunctions. In sharp contrast to the electronic states exhibited in Fig. 2f, g, these maps reveal that significant electronic state distributions occur at the edge of the GNRs-1 on the Cu(III). Meanwhile, the GNRs-1 on S-CuSe monolayer barely shows any signal of

electronic state distribution. It should be emphasized that the electronic states of the GNRs-1 on the Cu(III) are uniformly distributed throughout its entire skeleton, while those of the GNRs-1 on the S-CuSe monolayer are predominantly localized at the edges. The main reason behind this difference in the electronic state distributions of the GNRs-1 homojunctions lies in the orbital hybridization of GNRs-1 with Cu(III) and S-CuSe^{43,44}.

Synthesis of GNRs-1/S-CuSe heterostructures

After further increasing the deposition amount of Se atoms onto the above GNRs-1 homojunction sample and then annealing to 220 °C, all the GNRs-1 are intercalated by the S-CuSe monolayer, thereby forming high-quality and well-defined GNRs-1/S-CuSe heterostructures, as illustrated in Fig. 1e. Figure 3a, b displays a high-resolution STM image of GNRs-1/S-CuSe heterostructures and the corresponding structural model, respectively. At a specific bias voltage, the lattice of the S-CuSe can be mapped onto the backbone of

GNRs-1 (Supplementary Fig. 11). This indicates a weak interaction between GNRs-1 and S-CuSe. Additionally, by using a CO-functionalized tungsten tip, the structural arrangement of the S-CuSe and the GNRs-1 can be accurately resolved at the atomic scale (Fig. 3c), which can clearly distinguish that GNRs-1 maintain the same atomic structure characteristics.

Then, we shift to the investigation of the band alignment of the GNRs-1/S-CuSe vdWHs. Figure 3d shows the typical dI/dV spectra acquired at colored dots in Fig. 3a. Among these spectra, the two dI/dV spectra (Nos. #1 and #5) reveal the electronic properties of the S-CuSe monolayer on the Cu(111) substrate. These properties are consistent with those obtained on the clean S-CuSe monolayer (Supplementary Fig. 12). The VBM of S-CuSe monolayer locates at approximately -650 mV and the CBM at 950 mV, leading to a bandgap of 1.60 eV. The dI/dV spectra (Nos. #2 and #4) obtained at the edge of the GNRs-1 exhibit two distinct peaks, with a CBM at 630 mV and a VBM at -320 mV, which is further confirmed by the enlarged dI/dV spectra (Supplementary Fig. 13). Our experimental results suggest that GNRs-1 and its underlying semiconducting S-CuSe monolayer exhibit a straddling band alignment.

Different from the dI/dV spectra at the edge of the GNRs-1, the gray-colored dI/dV spectrum (No. #3) obtained at the center of GNRs-1 shows the two peaks at 920 mV and -680 mV (Fig. 3d), which can be assigned to the contribution from the underlying S-CuSe monolayer beneath the GNRs-1. According to previous reports¹⁶, the band gap opening in the GNRs arises from their edge effects and quantum confinement. For most experimentally synthesized GNRs, electronic states are predominantly localized at the edges. Consequently, the valence and conduction band edges of these GNRs are observable at the edges but not at the center. Compared to the dI/dV spectra (Nos. #1 and #5) obtained on the S-CuSe surface away from GNRs-1, an -30 mV shift to the left is observed, which can be ascribed to the charge transfer between the GNRs-1 and the S-CuSe monolayer. Regarding the band alignment of GNR-1/S-CuSe vdWHs, the schematic diagram is shown in Fig. 3f. (for more detailed information, please refer to Supplementary Fig. 14). Since the E_F of GNR-1 is higher than that of S-CuSe, when GNR-1 and S-CuSe come into contact to form a GNR-1/S-CuSe vdWHs, electrons are transferred from the GNR-1 to the S-CuSe, and consequently, the E_F of both eventually align to the same level. Due to the electron accumulation in the S-CuSe monolayer, its E_F shifts upward by 30 meV. The dI/dV maps obtained at bias voltages of -320 mV and 630 mV reveal strong electronic state aggregations at the zigzag edge of GNRs-1, which is consistent with the simulated maps of the conduction band and valence band of GNRs-1 (Fig. 3e). Moreover, the dI/dV map acquired at a bias voltage of 950 mV shows the electronic state aggregation for the S-CuSe monolayer, while the GNR-1 appears relatively dark in this region, as depicted in Supplementary Fig. 15.

Band alignments of 1D-GNR/2D-CuSe heterostructures

Finally, the S-CuSe monolayer converts into the N-CuSe monolayer by further increasing Se atoms onto the sample of GNR-1/S-CuSe vdWHs and then annealing to 220 °C, as shown in Fig. 1f. Noting that as the amount of Se deposition increases, some white spots appear on the GNRs edges, which may be caused by unreacted Se atoms or clusters onto the GNRs and CuSe monolayers. The dI/dV spectra of N-CuSe monolayer indicate that the bandgap of the N-CuSe monolayer is 2.49 eV, which is about 0.90 eV larger than that of the S-CuSe monolayer (Supplementary Fig. 16). Figure 4a presents a high-resolution STM image of GNRs-1/N-CuSe vdWHs. The dI/dV spectra in Fig. 4b demonstrate a straddling band alignment for GNRs-1/N-CuSe vdWHs. Compare to the GNRs-1/S-CuSe vdWHs, the bandgap of the GNRs-1 on the N-CuSe remains almost unchanged, yet the band structure shifts -100 mV to the right. The main reason for this shift is that there is more charge transfer occurring between the GNRs-1 and the N-CuSe.

The gray-colored dI/dV spectrum in Fig. 4b, acquired from the center of GNRs-1, exhibits two peaks at 1450 mV (CBM) and -940 mV (VBM). The orange-colored dI/dV spectra, obtained on the N-CuSe away from GNRs-1, shows two peaks at 1490 mV and -900 mV, respectively. Compared to the dI/dV spectrum acquired from the center of GNRs-1, the CBM and VBM of the dI/dV spectrum obtained at the N-CuSe away from GNRs-1 are shifted to the left by 40 mV overall. The schematic diagram is shown in Fig. 4c. The E_F of GNR-1 is higher than that of the N-CuSe. When the GNR-1 and the N-CuSe contact to form a GNR-1/N-CuSe vdWHs, the E_F of the GNR-1 and the N-CuSe eventually align to the same level with electrons transferring from GNR-1 to N-CuSe (Supplementary Fig. 17). Due to the electron accumulation in the N-CuSe, its E_F shift upward by 40 meV. Meanwhile, the GNR-1/N-CuSe vdWHs shows a straddling band alignment, like GNR-1/S-CuSe vdWHs.

In order to further construct diverse 1D-GNRs/2D-CuSe heterostructures, we have managed to fabricate two additional types of GNRs, namely GNR-2 and GNR-3, on the Cu(111) substrate. It is worth to emphasize that GNRs-3 has not been reported in previous literature. Subsequently, we carried out the CuSe monolayer intercalation process to lift these GNRs. The synthetic pathway and atomic structure of GNRs-2 and GNRs-3 are shown in Supplementary Fig. 18 and 19, respectively⁴⁵⁻⁴⁸. Compared to GNR-1, GNR-2 has the same edge structure but a narrower width, as illustrated in Fig. 4d. The experimental results indicate that GNR-2/S-CuSe vdWHs have staggered band alignments as shown in Fig. 4e and f. (the detailed information is shown in Supplementary Fig. 20 and 21). Compared to GNR-1, GNR-3 has the same width but a different edge structure, as illustrated in Figs. 4g and 4i. The experimental results indicate that both GNRs-3/S-CuSe and GNRs-3/N-CuSe vdWHs have straddling band alignment, as shown in Figs. 4h and 4j.

Our strategy involves the step-by-step reaction of Se atoms with Cu(111), demonstrating its capability to construct GNR homojunction precisely. Previous reports show that such GNRs homojunction has important insights for future electronic nanodevices, such as nanoscale light-controlled diode⁴⁸⁻⁵⁰ etc. The chemical potential difference of Se atoms in S-CuSe and N-CuSe indicates that the band arrangement of GNRs/CuSe heterojunction can be controlled using this strategy. Moreover, we found that the GNRs can also be synthesized directly onto CuSe substrate. The procedure involves first depositing DBBA molecules onto an S-CuSe/Cu(111) surface, followed by annealing the sample at 400 °C. At this temperature, the DBBA molecules undergo dehalogenation coupling and cyclodehydrogenation reactions. While CuSe exhibits weaker catalytic activity than Cu(111), $N=7$ and $N=14$ armchair graphene nanoribbons can still be successfully synthesized on the CuSe substrate (7-AGNRs and 14-AGNRs), as demonstrated in Supplementary Fig. 22a–c. Similarly, depositing DBBA molecules onto an N-CuSe/Cu(111) surface and annealing the sample at 400 °C yields 7-AGNRs (Supplementary Fig. 22d–e).

The strategy we proposed is not limited to the preparation of 1D-GNRs/2D-CuSe heterostructures, but also has broad reference value and significance for the preparation of heterostructures composed of other low-dimensional carbon materials (including 0D carbon quantum dots, 2D graphene or porous graphene) and 2D transition metal dichalcogenides (TMDs) materials. The proposed intercalation strategy has a broad application scope. It can be applied to both the construction of heterojunctions and facilitating the characterization of the intrinsic electrical properties of the products synthesized on the Cu(111) substrate. Currently, due to the strong orbital hybridization between the Cu(111) substrate and the synthesized products, most of the products synthesized on the Cu(111) substrate have difficulty in showing their inherent electronic properties³⁹⁻⁴¹. Until now, no effective intercalation method has been developed to adequately weaken this interaction. Our proposed intercalation strategy of 2D CuSe monolayer features relatively gentle growth conditions, which can effectively prevent the products from agglomerating and desorbing,

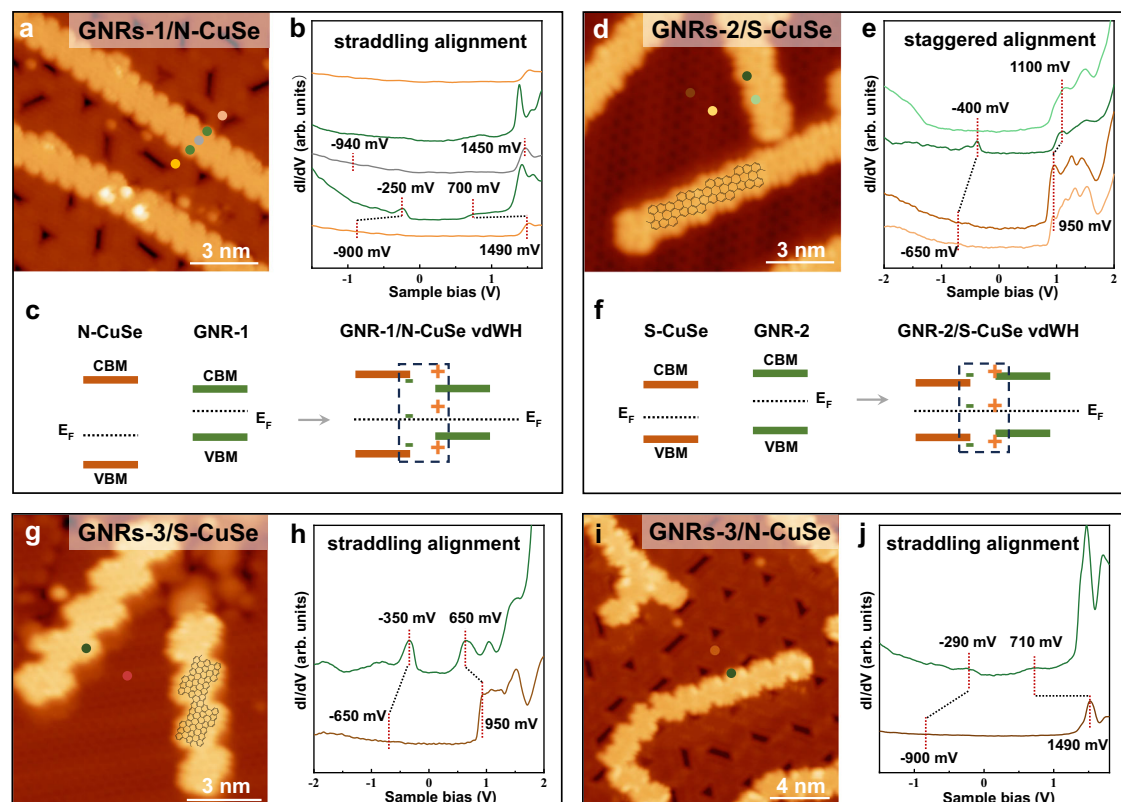


Fig. 4 | 1D GNRs/2D CuSe vdWHs with diverse band alignments. **a** High-resolution STM image of GNRs-1/N-CuSe vdWHs (Voltage = 0.2 V, I-setpoint = 50 pA). **b** dI/dV spectra of GNRs-1/N-CuSe vdWHs acquired at the colored dots in **(a)**. The vertical dashed lines represent the positions of the conduction band and the valence band in the dI/dV spectra. **c**, Schematic band-diagram illustration of GNRs-1/N-CuSe vdWHs. The + and - signs in dashed box represent positive and negative charges, respectively. **d** High-resolution STM image of GNRs-2/S-CuSe vdWHs (Voltage = 0.8 V, I-setpoint = 50 pA). **e** dI/dV spectra of GNRs-2/S-CuSe vdWHs acquired at the colored dots in **(d)**. The vertical dashed lines represent the positions of the conduction band and the valence band in the dI/dV spectra. **f** Schematic

band-diagram illustration of GNRs-2/S-CuSe vdWHs. The + and - signs in dashed box represent positive and negative charges, respectively. **g** High-resolution STM image of GNRs-3/S-CuSe vdWHs (Voltage = 0.65 V, I-setpoint = 200 pA). **h** dI/dV spectra of GNRs-3/S-CuSe vdWHs acquired at the colored dots in **(g)**. The vertical dashed lines represent the positions of the conduction band and the valence band in the dI/dV spectra. **i** High-resolution STM image of GNRs-3/N-CuSe vdWHs (Voltage = 0.2 V, I-setpoint = 80 pA). **j** dI/dV spectra of GNRs-3/N-CuSe vdWHs acquired at the colored dots in **(i)**. The vertical dashed lines represent the positions of the conduction band and the valence band in the dI/dV spectra.

thereby serving as an effective intercalation layer. Importantly, the intercalated CuSe monolayer significantly reduces the degree of orbital hybridization between the Cu(111) substrate and the product, which is quite beneficial for achieving a clearer characterization of the electronic structure. For instance, the dI/dV spectrum of GNRs-3 on the Cu(111) surface reveals that the peak is suppressed under negative bias voltage (Supplementary Fig. 23). In contrast, when examined on two CuSe monolayers, a distinct characterization is achieved, as illustrated in Fig. 4h and j.

Finally, we carry out the air stability experiment of the GNRs-1/CuSe heterostructure, the results are shown in Supplementary Fig. 24 and 25. Firstly, we transfer the GNRs-1/CuSe heterostructure sample from the vacuum to the atmosphere and carried out Raman characterization. As shown in Supplementary Fig. 24, we can only observe the two peaks near 1350 cm^{-1} and 1610 cm^{-1} due to the overly strong signal of Cu(111) substrate. The Raman spectrum is dominated by a peak at 1610 cm^{-1} that is related to the GNRs-1' sp^2 lattice (G mode)³¹. The peak at 1350 cm^{-1} (D mode) is related to the disordered vibration of GNRs-1. These two peaks are attributed to the characteristic peaks of GNRs-1 which is qualitatively consistent with the previous reports. And we did not observe the Raman characteristic peaks related to CuSe, which might be related to the overly strong background signal of the Cu(111) substrate. To further confirm the atmospheric stability of the synthesized GNRs-1/CuSe heterostructure, we transferred the GNRs-1/CuSe heterostructure samples exposed to the

atmosphere to a vacuum and annealed them at $200\text{ }^\circ\text{C}$ for 1 h. The experiment results in Supplementary Fig. 25 show that the GNR/CuSe heterostructure is stable after exposure to the atmosphere. The white bright spots at the edge of GNRs may be contaminants or impurities that were not removed during the annealing process.

In summary, we exhibit a synthesis strategy of GNRs homojunction and 1D-GNR/2D-CuSe heterostructures. STM, NC-AFM, DFT calculation confirm the effectiveness of this strategy. GNRs homojunction has a staggered gap, appearing as a p-n junction characteristic. 1D-GNR/2D-CuSe heterojunctions display a diverse band alignment, achieved by changing the width and edge topologies of GNRs or controlling the two distinct superstructures of CuSe. Our approach is expected to broaden the application scenarios of 1D/2D heterostructures in optoelectronics and catalysis.

Methods

Experimental details

STM measurements were performed with a commercial low-temperature STM from Scienta Omicron operating at 4.2 K and base pressures below 1×10^{-10} mbar. Cu(111) single crystal was cleaned by repeated Ar^+ sputtering and annealing cycles of 853 K. The synthetic routes of QA and TA were shown in Supplementary Figs. 26 and 27 (sublimed grade 98.00%, 99.00%, respectively). DBBA precursor and selenium elements were purchased from Bide Pharmatech Ltd. (sublimed grade 99.00%). All precursors and selenium atoms deposited via

a standard K-cell style molecular evaporator (molecular beam epitaxy), with chamber pressure lower than 1×10^{-9} mbar during the whole sublimation process. The deposition amounts of precursors and selenium element were controlled by the deposition time and temperature. All GNRs were grown in ultra-high vacuum ($p \leq 1 \times 10^{-9}$). All STM images were acquired in constant-current mode, and NC-AFM and HR-STM images were acquired in constant-height mode with a CO-functionalized tungsten tip. dI/dV measurements were performed using a lock-in amplifier with a modulation frequency of $f = 599$ Hz and modulation amplitude $V_{pk} = 25$ mV. dI/dV point spectra and maps were acquired under constant-current mode. All STM/NC-AFM images and dI/dV maps were processed with WSxM software⁵².

Computational methods

Density functional theory (DFT) based first principles calculations were performed in a plane-wave formulation with the projector augmented wave method (PAW)⁵³ as implemented in the Vienna Ab initio Simulation Package (VASP) code. The Perdew–Burke–Ernzerhof (PBE) parametrization of the generalized gradient approximation (GGA) was used⁵⁴. DFT-D3 method following Grimme's strategy was used for describing the long-range van der Waals interactions⁵⁵. The cutoff energy for the plane waves was 500 eV. The vacuum layer is larger than 15 Å between neighboring slabs⁵⁶. In relaxation, atoms in the bottom layer of the substrate were fixed and all the other atoms were relaxed until the atomic forces were less than 0.02 eV/Å.

Data availability

Relevant data supporting the key findings of this study are available within the article and the Supplementary Information file. All raw data generated during the current study are available from the corresponding authors upon request.

References

1. Li, D. et al. Two-dimensional non-volatile programmable p–n junctions. *Nat. Nanotechnol.* **12**, 901–906 (2017).
2. Xue, Y. et al. Scalable production of a few-layer MoS₂/WS₂ vertical heterojunction array and its application for photodetectors. *ACS Nano* **10**, 573–580 (2016).
3. Zhou, J. et al. A library of atomically thin metal chalcogenides. *Nature* **556**, 355–359 (2018).
4. Chang, C. et al. Recent progress on two-dimensional materials. *Acta Phys. Chim. Sin.* **37**, 2108017 (2021).
5. Withers, F. et al. Light-emitting diodes by band-structure engineering in Van der Waals heterostructures. *Nat. Mater.* **14**, 301–306 (2015).
6. Xu, H. et al. Van der Waals heterostructures for photoelectric, memory, and neural network applications. *Small Sci.* **4**, 2300213 (2024).
7. Islam, S. et al. Ultra-sensitive graphene–bismuth telluride nano-wire hybrids for infrared detection. *Nanoscale* **11**, 1579–1586 (2019).
8. Yang, Z. et al. High-performance photoinduced memory with ultrafast charge transfer based on MoS₂/SWCNTs network Van der Waals heterostructure. *Small* **15**, 1804661 (2019).
9. Ahmad, W. et al. Progress and insight of Van der Waals heterostructures containing interlayer transition for near infrared photodetectors. *Adv. Funct. Mater.* **33**, 2300686 (2023).
10. Oh, J. et al. Fabrication of a MoS₂/graphene nanoribbon heterojunction network for improved thermoelectric properties. *Adv. Mater. Inter.* **6**, 1901333 (2019).
11. Liu, Y. et al. Van der Waals heterostructures and devices. *Nat. Rev. Mater.* **1**, 1–17 (2016).
12. Son, Y.-W. et al. Half-metallic graphene nanoribbons. *Nature* **444**, 347–349 (2006).
13. Schwierz, F. Graphene transistors. *Nat. Nanotechnol.* **5**, 487–496 (2010).
14. Shen, Y.-T. et al. Switchable ternary nanoporous supramolecular network on photo-regulation. *Nano Lett.* **11**, 3245–3250 (2011).
15. Cai, J. et al. Atomically precise bottom-up fabrication of graphene nanoribbons. *Nature* **466**, 470–473 (2010).
16. Ruffieux, P. et al. Electronic structure of atomically precise graphene nanoribbons. *ACS Nano* **6**, 6930–6935 (2012).
17. Son, Y.-W. et al. Energy gaps in graphene nanoribbons. *Phys. Rev. Lett.* **97**, 216803 (2006).
18. Zhang, Y. et al. On-Surface Synthesis of a Nitrogen-Doped Graphene Nanoribbon with Multiple Substitutional Sites. *Angew. Chem. Int. Ed.* **61**, e202204736 (2022).
19. Chen, Y.-C. et al. Tuning the band gap of graphene nanoribbons synthesized from molecular precursors. *ACS Nano* **7**, 6123–6128 (2013).
20. Kolmer, M. et al. Rational synthesis of atomically precise graphene nanoribbons directly on metal oxide surfaces. *Science* **369**, 571–575 (2020).
21. Yamaguchi, J. et al. Small bandgap in atomically precise 17-atom-wide armchair-edged graphene nanoribbons. *Commun. Mater.* **1**, 36 (2020).
22. Fan, Q. et al. Biphenylene network: a nonbenzenoid carbon allotrope. *Science* **372**, 852–856 (2021).
23. Ruffieux, P. et al. On-surface synthesis of graphene nanoribbons with zigzag edge topology. *Nature* **531**, 489–492 (2016).
24. Rizzo, D. J. et al. Topological band engineering of graphene nanoribbons. *Nature* **560**, 204–208 (2018).
25. Zhang, H. et al. On-surface synthesis of rylene-type graphene nanoribbons. *J. Am. Chem. Soc.* **137**, 4022–4025 (2015).
26. Lei, Y. et al. Graphene and beyond: recent advances in two-dimensional materials synthesis, properties, and devices. *ACS Nanosci. Au* **2**, 450–485 (2022).
27. Borin, B. G. et al. Growth optimization and device integration of narrow-bandgap graphene nanoribbons. *Small* **18**, 2202301 (2022).
28. Mutlu, Z. et al. Contact engineering for graphene nanoribbon devices. *Appl. Phys. Rev.* **10**, 041412 (2023).
29. Rizzo, D. J. et al. Length-dependent evolution of type II heterojunctions in bottom-up-synthesized graphene nanoribbons. *Nano Lett.* **19**, 3221–3228 (2019).
30. Bronner, C. et al. Aligning the band gap of graphene nanoribbons by monomer doping. *Angew. Chem. Int. Ed.* **52**, 4422–4425 (2013).
31. Cai, J. et al. Graphene nanoribbon heterojunctions. *Nat. Nanotechnol.* **9**, 896–900 (2014).
32. Blankenburg, S. et al. Intraribbon heterojunction formation in ultranarrow graphene nanoribbons. *ACS Nano* **6**, 2020–2025 (2012).
33. Wang, D. et al. Twisted bilayer zigzag-graphene nanoribbon junctions with tunable edge states. *Nat. Commun.* **42**, 1018 (2023).
34. Lin, X. et al. Intrinsically patterned two-dimensional materials for selective adsorption of molecules and nanoclusters. *Nat. Mater.* **16**, 717–721 (2017).
35. Gao, L. et al. Epitaxial growth of honeycomb monolayer CuSe with Dirac nodal line fermions. *Adv. Mater.* **30**, 1707055 (2018).
36. Niu, G. et al. Se-concentration dependent superstructure transformations of CuSe monolayer on Cu (111) substrate. *2D Mater.* **9**, 015017 (2021).
37. Wang, X. et al. Structural characterizations and electronic properties of CuSe monolayer endowed with triangular nanopores. *J. Mater. Sci.* **56**, 10406–10413 (2021).
38. Niu, G. et al. Electronic properties of monolayer copper selenide with one-dimensional moiré patterns. *Front. Phys.* **18**, 13303 (2023).
39. Mishra, S. et al. Synthesis and characterization of [7] triangulene. *Nanoscale* **13**, 1624–1628 (2021).
40. Han, P. et al. Self-assembly strategy for fabricating connected graphene nanoribbons. *ACS Nano* **9**, 12035–12044 (2015).

41. Jacobse, P. H. et al. Mapping the conductance of electronically decoupled graphene nanoribbons. *ACS Nano* **12**, 7048–7056 (2018).
42. Gosavi, S. et al. Physical, optical and electrical properties of copper selenide (CuSe) thin films deposited by solution growth technique at room temperature. *J. Alloy. Compd.* **448**, 344–348 (2008).
43. Alabugi, I. et al. Orbital hybridization: a key electronic factor in control of structure and reactivity. *J. Phys. Org. Chem.* **28**, 147–162 (2015).
44. Trindle, C. et al. Local orbital and bond index characterization of hybridization. *J. Am. Chem. Soc.* **91**, 853–858 (1969).
45. Li, J. et al. Topological phase transition in chiral graphene nanoribbons: from edge bands to end states. *Nat. Commun.* **12**, 5538 (2021).
46. Lawrence, J. et al. Circumventing the stability problems of graphene nanoribbon zigzag edges. *Nat. Chem.* **14**, 1451–1458 (2022).
47. Han, P. et al. Bottom-up graphene-nanoribbon fabrication reveals chiral edges and enantioselectivity. *ACS Nano* **8**, 9181–9187 (2014).
48. Guo, Y. et al. Doped GNR p-n junction as high performance NDR and rectifying device. *J. Phys. Chem. C.* **116**, 18064–18069 (2012).
49. Zhang, Y. et al. Organic single-crystalline p-n junction nanoribbons. *J. Am. Chem. Soc.* **132**, 11580–11584 (2010).
50. Guo, Y. et al. Light-controlled organic/inorganic p-n junction nanowires. *J. Am. Chem. Soc.* **130**, 9198–9199 (2008).
51. Barin, B. G. et al. On-surface synthesis and characterization of teranthene and hexanthene: ultrashort graphene nanoribbons with mixed armchair and zigzag edges. *Nanoscale* **15**, 16766–16774 (2023).
52. Horcas, I. et al. WSXM: A software for scanning probe microscopy and a tool for nanotechnology. *Rev. Sci. Instru.* **78**, 013705 (2007).
53. Kresse, G. et al. Efficient iterative schemes for ab initio total-energy calculations using a plane-wave basis set. *Phys. Rev. B* **54**, 11169 (1996).
54. Perdew, J. et al. Generalized gradient approximation made simple. *Phys. Rev. Lett.* **77**, 3865 (1996).
55. Grimme, S. et al. A consistent and accurate ab initio parametrization of density functional dispersion correction (DFT-D) for the 94 elements H-Pu. *J. Chem. Phys.* **132**, 154104 (2010).
56. Grimme, S. et al. Effect of the damping function in dispersion corrected density functional theory. *J. Comput. Chem.* **32**, 1456–1465 (2011).

Acknowledgements

This work was supported by the National Key R&D Program of China (No. 2024YFA1207800); the National Natural Science Foundation of China (Nos. 62271238, 22372074, 62301240), Yunnan Fundamental Research Projects (Nos. 202201AT070078, 202501AV070002, 202201BE070001-009 and 202301AW070017), the Major Basic Research Project of Science and Technology of Yunnan (202302AG050007), Yunnan Innovation Team of Graphene Mechanism Research and Application Industrialization (202305AS350017), Graphene Application and Engineering Research Center of Education Department of Yunnan Provi-

dence (KKPP202351001). Numerical computations were performed at Hefei Advanced Computing Center.

Author contributions

Y.Z., J.C.L. and L.G. contributed equally to this work. J.M.C. and J.C.L. conceived and coordinated the research project. Y.Z., G.F.N., Yi.Z., S.C.L., and Y.H. performed the growth and characterization. L. G. and X. G. carried out theoretical calculations under the guidance of S. X. D., X. J. Z. carried out molecular synthesis under the guidance of Y. Z. T., Yong Zhang, J. C. L., L. G., and J. M. C. drafted and edited the manuscript. All authors participated in discussing the data.

Competing interests

The authors declare no competing interests.

Additional information

Supplementary information The online version contains supplementary material available at <https://doi.org/10.1038/s41467-025-60916-w>.

Correspondence and requests for materials should be addressed to Jianchen Lu, Lei Gao, Xin-jing Zhao, Shixuan Du or Jinming Cai.

Peer review information *Nature Communications* thanks Zafer Mutlu, who co-reviewed with Muhammed YusufogluXufan Li; and Bosai Lyu for their contribution to the peer review of this work. A peer review file is available.

Reprints and permissions information is available at <http://www.nature.com/reprints>

Publisher's note Springer Nature remains neutral with regard to jurisdictional claims in published maps and institutional affiliations.

Open Access This article is licensed under a Creative Commons Attribution-NonCommercial-NoDerivatives 4.0 International License, which permits any non-commercial use, sharing, distribution and reproduction in any medium or format, as long as you give appropriate credit to the original author(s) and the source, provide a link to the Creative Commons licence, and indicate if you modified the licensed material. You do not have permission under this licence to share adapted material derived from this article or parts of it. The images or other third party material in this article are included in the article's Creative Commons licence, unless indicated otherwise in a credit line to the material. If material is not included in the article's Creative Commons licence and your intended use is not permitted by statutory regulation or exceeds the permitted use, you will need to obtain permission directly from the copyright holder. To view a copy of this licence, visit <http://creativecommons.org/licenses/by-nc-nd/4.0/>.

© The Author(s) 2025